Efficient Sensing of Selected Amino Acids as Biomarker by Green Phosphorene Monolayers: Smart Diagnosis of Viruses

Puspamitra Panigrahi,* Yash Pal, Akshaya Panigrahi, Hyeonhu Bae, Hoonkyung Lee, Rajeev Ahuja, and Tanveer Hussain*

Effective techniques for the detection of selected viruses detection of their amino acids (AAs) constituents are highly desired, especially in the present COVID pandemic. Motivated by this, we have used density functional theory (DFT) simulations to explore the potential applications of green phosphorene monolayer (GPM) as efficient nanobio-sensor. We have employed van der Waals induced calculations to study the ground-state geometries, binding strength, electronic structures, and charge transfer mechanism of pristine, vacancy-induced and metal-doped GPM to detect the selected AAs, such as glycine, proline and aspartic, in both aqueous and non-aqueous media. We find that the interactions of studied AAs are comparatively weak on pristine (−0.49 to −0.76 eV) and vacancy-induced GPM as compared to the metal-doped GPM (−0.62 to −1.22 eV). Among the considered dopants, Ag-doping enhances the binding of AAs to the GPM stronger than the others. In addition to appropriate binding energies, significant charge transfers coupled with measurable changes in the electronic properties further authenticate the potential of GPM. Boltzmann thermodynamic analysis have been used to study the sensing mechanism under varied conditions of temperatures and pressure for the practical applications. Our findings signify the potential of GPM based sensors towards efficient detection of the selected AAs.

1. Introduction

Due to the exceptional, tunable electrochemical, optical, and physical properties, various ultrathin 2D nanomaterials with unique anisotropic electron transport behavior turn out to be highly promising materials for biosensing applications.[1,2] Recently, various emerging 2D materials are being widely investigated as nanoplatforms for drug delivery, cancer therapy, bio-imaging, and as biosensors.[3] However, when it comes to nanosensors to detect a virus, which is a small collection of genetic code of either DNA or RNA, surrounded by a protein coat and can only replicate within a host organism, is so far less explored.[4] The simplest virus can have enough of RNA or DNA to encode four proteins, whereas a complex virus can encode up to 200 proteins.[5,6] These proteins play a major role for the virus to infect, replicate, spread, and modulate the host immune response. The building blocks of these proteins are assembled with 20 different amino acids (AAs), which are small

P. Panigrahi
Centre for Clean Energy and Nano Convergence
Hindustan Institute of Technology and Science
Chennai, Tamilnadu 603103, India
E-mail: puspamitrap@hindustanuniv.ac.in
Y. Pal
School of Aeronautical Sciences
Hindustan Institute of Technology and Science
Chennai, Tamilnadu 603103, India
A. Panigrahi
Central Institute of Brackishwater Aquaculture (ICAR-CIBA)
75 Santhome High Road, Chennai, Tamilnadu 600028, India

H. Bae, H. Lee
Department of Physics
Konkuk University
9
Seoul 0502, Republic of Korea
R. Ahuja
Condensed Matter Theory Group
Department of Physics and Astronomy
Uppsala University
Box 516, Uppsala S-75120, Sweden
R. Ahuja
Department of Physics
Indian Institute of Technology
Ropar, Rupnagar, Punjab 140001, India
T. Hussain
School of Chemical Engineering
The University of Queensland
Queensland
St Lucia, Brisbane 4072, Australia
E-mail: tanveer.hussain@une.edu.au

**ADVANCED
SCIENCE NEWS**

www.advancedsciencenews.com

**ADVANCED
THEORY AND
SIMULATIONS**

www.advtheorysimul.com

organic molecules having a unique side chain. Out of the 20, Gly (NH_2-CH_2-COOH) and Pro ($C_5H_9NO_2$) are the conditionally nonessential AAs whereas Asp ($C_4H_7NO_4$) is the nonessential one. There are many reports indicating the major mutation in the SARS-CoV-2's viral envelope spike protein, which is responsible for the attachment of the virus to the host, occurs by the substitution between amino acids like aspartate Asp-(D) and glycine (G).[7,8]

Among these three important AAs, Gly is a colorless, sweet-tasting crystalline solid, which can fit into both hydrophilic and hydrophobic environments due to its minimal side chain of only one hydrogen atom. Very recently, it is identified that in a mutant strain of SARS-CoV 2, the Gly substitutes the aspartic acid of spike glycoprotein at 614 position (D614G).[9] Pro is the only AAs, where the side chain is connected to the protein backbone twice while forming a five-membered nitrogen-containing ring. Whereas, Asp, which has an average occurrence of about 5% in most of the proteins, is hydrophilic and its sidechains are often hydrogen bonded. It is important to mention that Gly, Pro, and Asp are the most important AAs, which are distinctly present in proteins of some specific viruses like Influenza, HIV, SARS-CoV-2, and MERS-CoV. Therefore, it is crucial to identify these three AAs for the efficient detection of different viruses. Various mutant varieties of viruses, which can be detected by specific active sites of the amino acids, are the major focus of our present investigation.

In the current pandemic situation, it is difficult to detect all the mutant strains of a virus through conventional polymerase chain reaction techniques because of the volume of samples and cost involved. Moreover, the challenges in virus detection also include assay sensitivity, time duration, competency of staffs, and sample characteristics. As an alternative diagnostic tool, the virus-specific amino acids can rather be detected with highly sensitive nanobiosensors. In this regard, a specific type of peptide conjugated with gold nanoparticles was reported to be used for virus diagnosis.[10] In a similar context, Au and iron-oxide magnetic nanoparticle decorated carbon nanotubes (CNTs) were reported to be used for influenza and norovirus DNA sensing.[11]

Recently, several nanostructures have also been successfully used for the detection of various biomarkers[12,13] for the early detection and diagnosis. The nanomaterial-based sensors with their unique electro-chemical properties will bring advancement to diagnosis process by making the sensors minimally invasive and the same time extremely sensitive.[14,15] The surface chemistry of various 2D materials can be altered over functionalization or defect engineering to tune their electronic and optical properties while making these tailored 2D nanostructures best possible candidates for selective and effective sensing of various biomolecules.[16–18]

Carbonaceous nanostructures, such as graphene, carbon nanotube/boron nitride nanotube (CNT/BNT), and graphene-oxide (rGO) thin films with Ag/Au nanocomposites, having high electron mobility, are reported to have greater sensitivities, selectivities, and fast response time toward specific biomolecules.[19–22] Further, functionalized CNT and graphene, endowed with large surface area and loading capacity exhibit outstanding signal enhancement for biomolecular detection and are proposed as the practical point-of-care version of biosensors.[23] Even non-carbonaceous nanostructures like silica, indium tin oxide, and some organic polymers, having unique abilities for electron transfer, catalytic activity, and being biocompatible show promising biosensing approaches.[24–27] Very recently, both carbonaceous and noncarbonaceous 2D nanosheets have shown great potential in sensing various hazard gas molecules as well as biomolecules.[28,29] With unique physical and chemical properties, several 2D transition metal dichalcogenides are also reported with diverse range of biomedical applications like biosensors, drug delivery carriers, and also as therapeutic agents.[30,31] Recently, MoS_2-based ultrathin, highly flexible, wearable tactile sensor has been reported with wide sensing range and small response time.[32] Among the latest 2D sheets attracting attention as biosensors, MXenes are of the best materials with high conductivity, superior fluorescent, optical, and with plasmonic properties.[33]
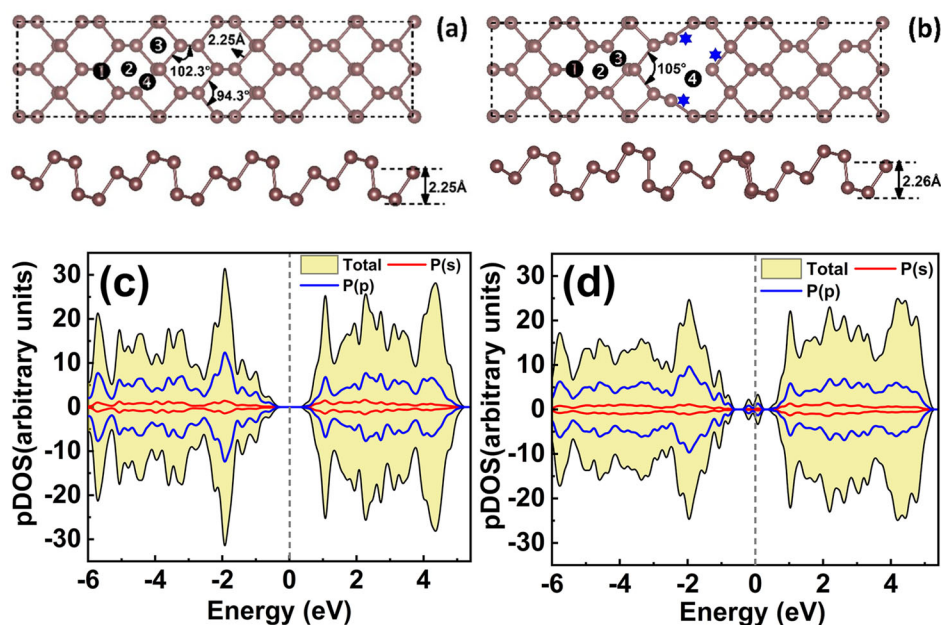
Nevertheless, for obtaining the fingerprints of different AAs, fluorescent and colorimetric methods have been used.[34] Years back, thiol-modified gold nanoparticles as a colorimetric sensor was reported for sensing few selected AAs in the presence of water.[35] Recently, the interactions between CuO nanoparticles with a set of natural AAs getting strongly influenced by the nature of their side chains were reported.[36] Although the applications of nanomaterials in sensing various biomolecules are rapidly increasing, however their electronic structures and atomistic behaviors, which ultimately influence their effective applicability, are poorly understood. However, recently emerging 2D phosphorene sheets which exist in three allotropic forms (blue, green, and black)[37] have sparked a surge of research in sensing applications as it possesses exceptionally higher surface to volume ratio due to its "puckered" lattice structure compared to its other 2D counterparts.[38–40] Very recently, a black phosphorus-based nanobiosensor has been reported for cancer diagnosis.[41] Among the three, the green phosphorene monolayer (GPM) which is direct band gap semiconductor with anisotropic carrier mobility[42] has been reported as a superior chemical gas-sensing material.[43]

In this work, by using first-principles density functional theory (DFT) simulations, we focus on the selective sensing propensity of novel GPM toward Gly, Pro, and Asp, in both aqueous and nonaqueous media. Further, the electronic properties and surface chemistry of the GPM have been modulated with vacancy defects and suitable substitutional dopants like Ag, Cu, and Zn to enhance the sensitivity toward the mentioned AAs. For practical applications, thermodynamic analysis is employed to explore the sensing mechanism at varied pressure/temperature conditions.

2. Methodology

First-principles DFT calculations were carried out within the projected augmented wave method with generalized gradient approximation by taking Perdew–Burke–Ernzerhof exchange functional as implemented in the VASP package.[44–48] For reliable binding mechanism, we employed the dispersion-corrected

T. Hussain
School of Science and Technology
University of New England
Armidale, New South Wales 2351, Australia

ADVANCED
SCIENCE NEWS
www.advancedsciencenews.com

ADVANCED
THEORY AND
SIMULATIONS
www.advtheorysimul.com

Figure 1. a,b) Top and side views of the optimized structures of GPM and GPM$_{vac}$ {brownish crimson color: P}, P—P, bond lengths, buckling parameter, and bond angles. Four black marks and three blue marks represent the investigated binding sites for GPM and GPM$_{vac}$ amino acid adsorption, respectively. c,d) Partial density of states (PDOS) of GPM and GPM$_{vac}$. The gray dotted line represents the Fermi level.

DFT-D3[49] method of Grimme, for calculating the ground-state electronic structures and energetics of the studied systems. A 4×2×1 supercell geometry of GPM was constructed while taking 15 Å vacuum space along perpendicular to the sheet to prevent coupling between the periodic images. For ground-state structure optimization, the Brillouin zone sampling was performed with a K-space grid of 3×3×1 within the Monkhorst–Pack scheme[50] and a denser K-point grid of 5×5×1 was chosen for the electronic properties. The energy cut-off for the plane wave basis-set was chosen at an optimized value of 500 eV. For structure optimization, the atomic positions and lattice parameters are optimized with an energy convergence criterion of 10^{-5} eV between two ionic steps and the forces are converged with the maximum force on each atom to be 0.001 eV A^{-1}.

The adsorption energies (E_{ads}) of the AAs over GPM are estimated as follows

$$E_{ads} = E_{S-AAs} - E_S - E_{AAs} \qquad (1)$$

here the 1st, 2nd, and 3rd terms present the total energies of the pristine or defected/doped GPM loaded with AAs, pristine (GPM), vacancy-induced (GPM$_{vac}$), and doped (GPM-M) without AAs, and that of the individual AAs molecules, respectively.

The planner average of the electrostatic potential $V(x, y, z)$ on a real space grid averaged over the 2D plane (surface normal is along the z-axis) GPM, GPM$_{vac}$, and GPM-M sheets can be estimated as Equation (2)[51]

$$\bar{V}(z) = \frac{1}{A} \int \int_{cell} V(x, y, z) dx dy \qquad (2)$$

here A is the area of the modeled GPM. While plotting $\bar{V}(z)$ as a function of z, one can extract $V(\infty)$, the electrostatic potential in

a vacuum. Then the surface work function ω_f, which is defined as the minimum energy required to move the electron from surface to the vacuum, is expressed as Equation (3)

$$\omega_f = V(\infty) - \varepsilon_f \qquad (3)$$

here $V(\infty)$ and ε_f represent the electrostatic potential of an electron at the point far from the target surface (vacuum) and at the Fermi level of the system, respectively.

The implicit solvation method (ISM) is often a realistic approach to calculating the energetics of solute–solvent interaction in any chemical process where the solvent with a specific dielectric constant is treated as a continuous medium. The dielectric constant of the solvent is considered as a powerful predictor for the polar contribution to the free energy calculation with ISM. Here using the VASP code, the ISM is used while using water as a continuous medium and surrounding the AAs and GPM to calculate the effects of water on the AAs molecules and crystal surfaces of GPM as well as the corresponding reaction barriers. The ISM treats the solute (both AAs and GPM) quantum mechanically. It treats solvent (water) as a continuum while including the effects of ionic solution at a first principle level, which is considered a more realistic simulation at an electrochemical interface.[52]

3. Results and Discussion

3.1. Structural Analysis and Adsorption of AAs on GPM/GPM$_{vac}$

The optimized structures and corresponding spin-polarized density of states (DOS) of GPM and GPM$_{vac}$ are presented in **Figure 1**a–d. The optimized structure of a unit cell of GPM contains six P atoms (see Table S1 and Figure S1, Supporting
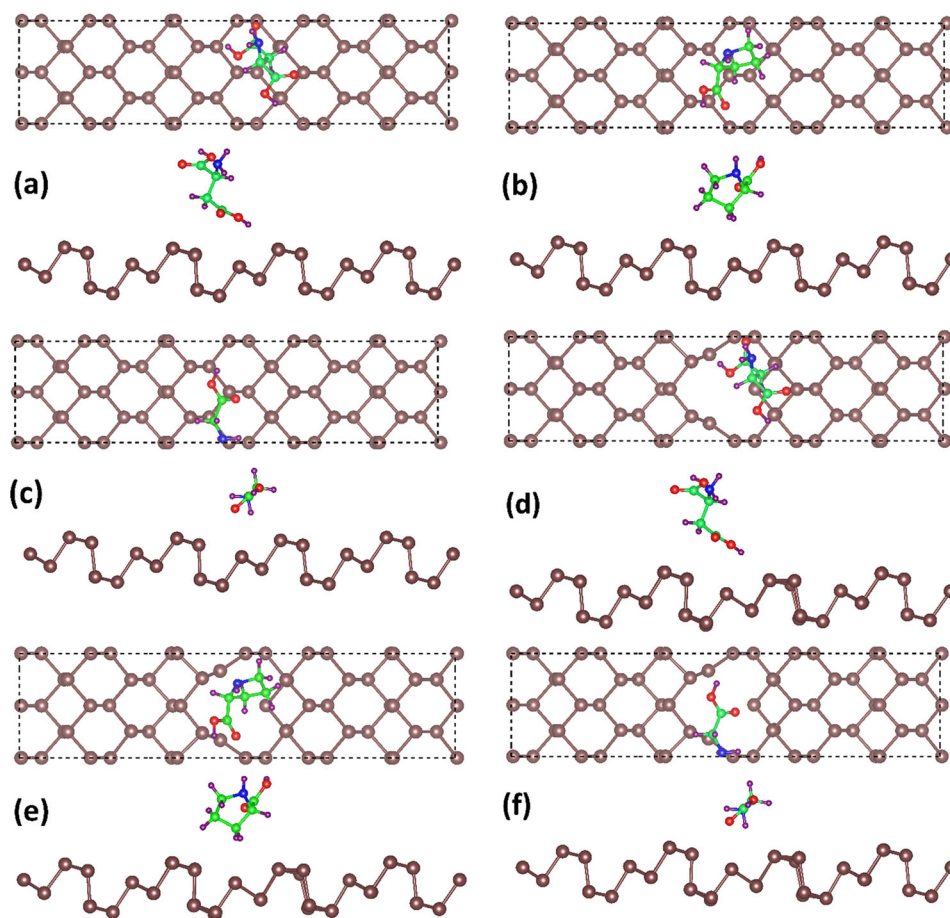
Figure 2. Top and side views of the optimized structures of Asp, Pro, and Gly adsorbed a–c) GPM and d–f) GPM$_{vac}$, respectively. (Brownish crimson: P, green: carbon, blue: nitrogen, red: oxygen, maroon: hydrogen.)

Information). GPM has a puckered honeycomb structure with each P atom covalently bonded with three adjacent atoms. The optimized lattice vectors of GPM are $a = b = 7.273$ Å. The optimized P—P bond length and P—P—P bond angles are calculated as 2.25 Å, and 102.3°, respectively, which agrees well with the literature.[53,54] Mild structural distortion in both bond length (2.26 Å) and bond angle (105°) are evident near the vacancy-induced region in GPM$_{vac}$, as shown in Figure 1b. We find that the pristine GPM is semiconducting in nature with distinct band-gap energy of ≈0.5 eV, however GPM$_{vac}$ turns out to be metallic, as shown in Figure 1c,d.

The P vacancy introduces unsaturated dangling bonds in GPM$_{vac}$, which resulted a semiconductor to metal transition. Such transitions in the electronic properties have already been reported in other 2D monolayers.[55] In the next step, both GPM and GPM$_{vac}$ are exposed to Gly, Pro, and Asp by considering the available binding sites and different orientations of the incident AAs.

A series of systematic calculations have been performed to identify the exact orientation and position of each AA w.r.t the proposed GPM sheet. The H-face, O-face of AAs are positioned w.r.t the sheet and the energetics were calculated (Table S2, Supporting Information). The best possible orientation for each case

was taken for further studies. Further, the entire structure was allowed to relax while keeping shape and volume of the supercell fixed. All the atoms of both the sheets and AA molecules are allowed to fully relax to obtain the ground state-optimized structures of each adsorbed configuration.

The optimized structures of the AAs-adsorbed monolayers, Asp-GPM, Pro-GPM, Gly-GPM, and Asp-GPM$_{vac}$, Pro-GPM$_{vac}$, Gly-GPM$_{vac}$ are presented in **Figure 2**a–f, respectively. The corresponding E_{ads} are summarized in **Table 1**. From the ground-state energetics, it is revealed that the H-face of Asp and Pro prefers to bind on the GPM and GPM$_{vac}$ sheet whereas, O-face of Gly point toward the GPM and GPM$_{vac}$ (Figure 2a–f). Additionally, Table 1 summaries the optimal binding distances, which are the shortest distances between the binding sites of the AAs from both GPM and GPM$_{vac}$.

From Table 1, it can be seen that the three mentioned AAs bind to GPM and GPM$_{vac}$ with substantial E_{ads} values in the range of −0.49 to −0.76 eV. The E_{ads} values of all the three AAs do not differ significantly on GPM and GPM$_{vac}$ (Table 1). The spin-polarized DOS of GPM and GPM$_{vac}$ adsorbed with the AAs are presented in **Figure 3**a–f.
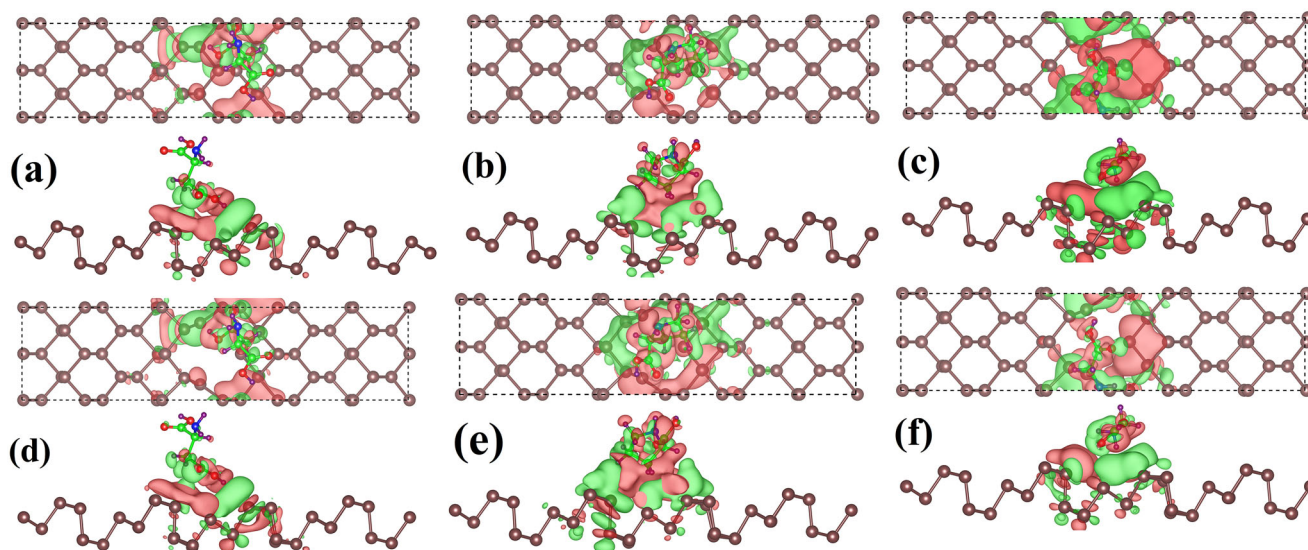
It can be seen that upon the AAs adsorption, both the GPM and GPM$_{vac}$ maintain their semiconducting and conducting

**ADVANCED
SCIENCE NEWS**

www.advancedsciencenews.com

**ADVANCED
THEORY AND
SIMULATIONS**

www.advtheorysimul.com

Table 1. The binding distance (Δd), adsorption energies (E_{ads}), and net charge transfer ($\Delta \rho$) between the AAs and the GPM/GPM$_{vac}$. A positive (negative) indicates a loss (gain) of electrons from each amino acid to the GPM sheet.

Amino acids	GPM			GPM$_{Vac}$			Ag@GPM			Cu@GPM			Zn@GPM		
	Δd [Å]	E_{ads} [eV]	$\Delta \rho$ [e]	Δd [Å]	E_{ads} [eV]	$\Delta \rho$ [e]	Δd [Å]	E_{ads} [eV]	$\Delta \rho$ [e]	Δd [Å]	E_{ads} [eV]	$\Delta \rho$ [e]	Δd [Å]	E_{ads} [eV]	$\Delta \rho$ [e]
Asp	2.53	−0.49	−0.06	2.57	−0.53	−0.06	2.66	−0.82	0.311	2.58	−0.59	0.359	2.49	−0.58	0.411
Pro	2.86	−0.59	−0.02	2.78	−0.56	−0.03	2.70	−0.62	0.204	3.14	−0.61	0.253	2.81	−0.59	0.320
Gly	2.96	−0.76	−0.04	2.83	−0.74	−0.09	2.25	−1.22	0.314	1.98	−0.89	0.189	3.26	−0.78	0.356
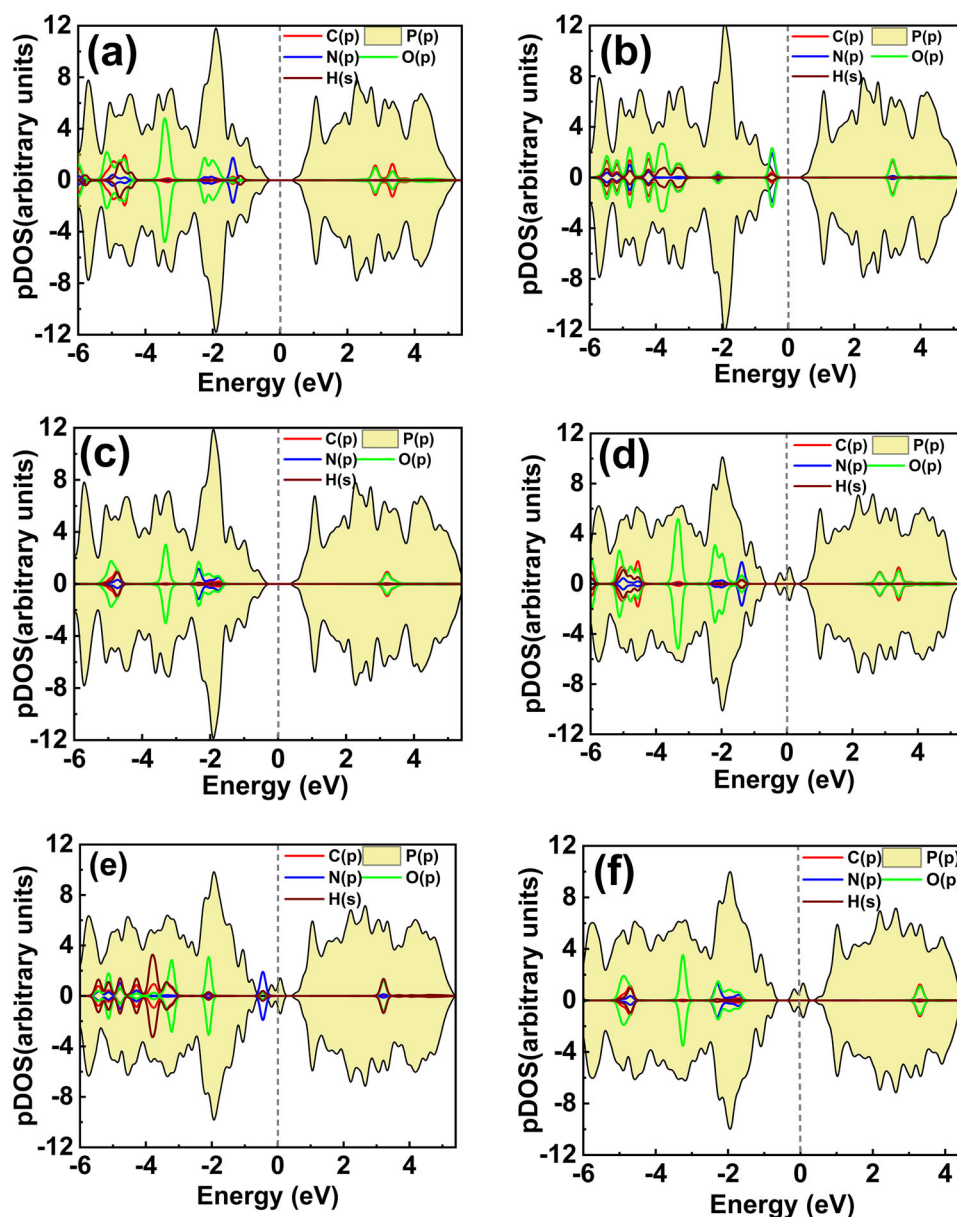
Figure 3. Density of states of a–c) GPM and d–f) GPM$_{vac}$ adsorbed with Asp, Pro, and Gly, respectively. The green dotted line represents the Fermi level.

**ADVANCED
SCIENCE NEWS**
www.advancedsciencenews.com

**ADVANCED
THEORY AND
SIMULATIONS**
www.advtheorysimul.com

Figure 4. Top and side views of the isosurface charge density plots of a–c) GPM and d–f) GPM_{vac} adsorbed with Asp, Pro, and Gly, respectively. The isovalue is taken as 0.005 e Å^{-3}. Green: charge depletion and red: charge accumulation. (Brownish crimson: P, green: carbon, blue: nitrogen, red: oxygen, maroon: hydrogen.)

characters, respectively (see Figure 3). In the case of Asp (Gly)-GPM, the N 2p and O 2p bands hybridizing with P 2p bands, which are located within the valance band region of GPM/GPM_{vac} whereas for Pro-GPM, the hybrid bands rather play a dominant role near the Fermi level. For both, Asp-GPM and Gly-GPM, there are no additional bands in the bandgap region of GPM/GPM_{vac}, which indicates the interaction of both the AAs with GPM/GPM_{vac}, is mainly due to the hybridization between the p-states (N 2p and O 2p) of AAs with lone pair electrons of the p-states of the GPM/GPM_{vac}. Whereas, for Pro-GPM, the impurity bands from N 2p and O 2p states are predominant near the Fermi level. For Pro-GPM, the n-type bands are generated due to the strong electron-donating ability of Pro to the GPM/GPM_{vac}. However, it is interesting to see that for Gly, the E_{ads} to GPM/GPM_{vac} is stronger (−0.76/−0.74 eV) compared to that of Asp and Pro (−0.49/−0.53 and −0.59/−0.56 eV), which can be attributed to the dipole–dipole interaction between the Pro and GPM/GPM_{vac}.[56]

Further, to understand the strong E_{ads} values of AAs on GPM/GPM_{vac}, we have performed Bader charge analysis to learn about the net charge transfer, which is summarized in Table 1. For qualitative analysis, we have used the following relation to explore the isosurface charge densities

$$\Delta\rho = \rho_{(S-AAs)} - \rho_S - \rho_{AAs} \tag{4}$$

here 1st, 2nd, and 3rd terms are the total charge densities of AAs-adsorbed GPM/GPM_{vac}, bare GPM/GPM_{vac}, and that of individuals AAs, respectively. The corresponding charge density plots are presented in **Figure 4**.

From the Bader analysis, it is revealed that all the three AAs lose their electronic charges to the P atoms of GPM/GPM_{vac}, which are in the vicinities of Asp, Pro, and Gly, see Figure 4a–f. The transfer of charge from the AAs to the GPM/GPM_{vac} results in a reasonably strong E_{ads} values as given in Table 1.
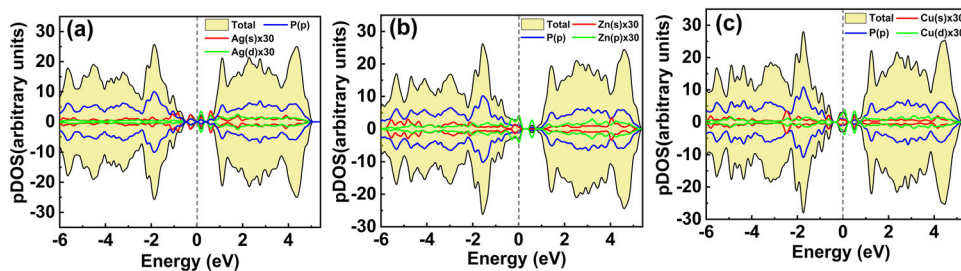
3.2. Adsorption of AAs on GPM-M

Significant improvement in sensing performance of various 2D dichalcogenides over surface functionalization with suitable metal nanoparticles has been reported elsewhere.[57] Following this, we have doped GPM with selected dopants (Ag, Cu, Zn) separately, which results into the formation of Ag@GPM, Cu@GPM, and Zn@GPM, respectively. The formation energies (E_f) of these substitutions are calculated to be −2.6, −4.8, and −1.8 eV for Ag@GPM, Cu@GPM, and Zn@GPM, respectively. Owing to the outermost electronic configurations and atomic sizes, the studied dopants can change the symmetry and alter the electronic properties of the GPM-M, which can influence the bandgap, electron mobility, spin densities of the sheet. The SP-DOS plots of the Ag@GPM, Cu@GPM, and Zn@GPM are presented in **Figure 5**a–c.

Doped with electron-surplus metals, the Ag@GPM, Cu@GPM, and Zn@GPM systems are turned out to be metallic as shown in Figure 5a–c. Though, with metal doping it was expected to get localized states, which can induce spin density to the doped sheets, for all the three doped sheets M-GPM (M: Ag, Zn, Cu), the spin-polarized ground-state optimization calculations reveal symmetry in both spin-up and spin-down states, confirming paramagnetic states.

Next, the AAs were introduced at the available binding sites over Ag@GPM, Cu@GPM, and Zn@GPM and the systems were fully optimized. The ground-state geometries, spin-polarized DOS, and charge density plots of AAs-adsorbed Ag@GPM are presented in **Figure 6** and Figures S2 and S3 in the Supporting Information. The corresponding E_{ads} values are summarized in Table 1.

The E_{ads} values of Asp, Pro, and Gly on Ag@GPM are calculated as −0.82, −0.62, and −1.22 eV, respectively, whereas the corresponding Δd values as 2.2, 2.7, and 2.6 Å, respectively. It is evident that the E_{ads} values of AAs on Ag@GPM are much stronger

ADVANCED
SCIENCE NEWS
www.advancedsciencenews.com

ADVANCED
THEORY AND
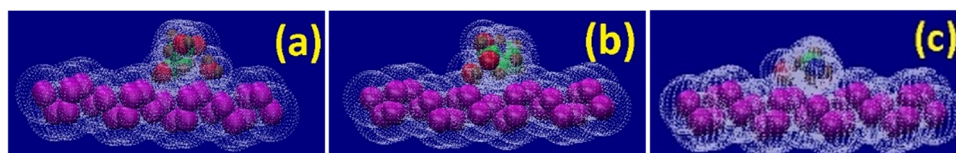**SIMULATIONS**
www.advtheorysimul.com

Figure 5. Spin-polarized density of states of a) Ag@GPM, b) Zn@GPM, and c) Cu@GPM. The gray dotted line represents the Fermi level.
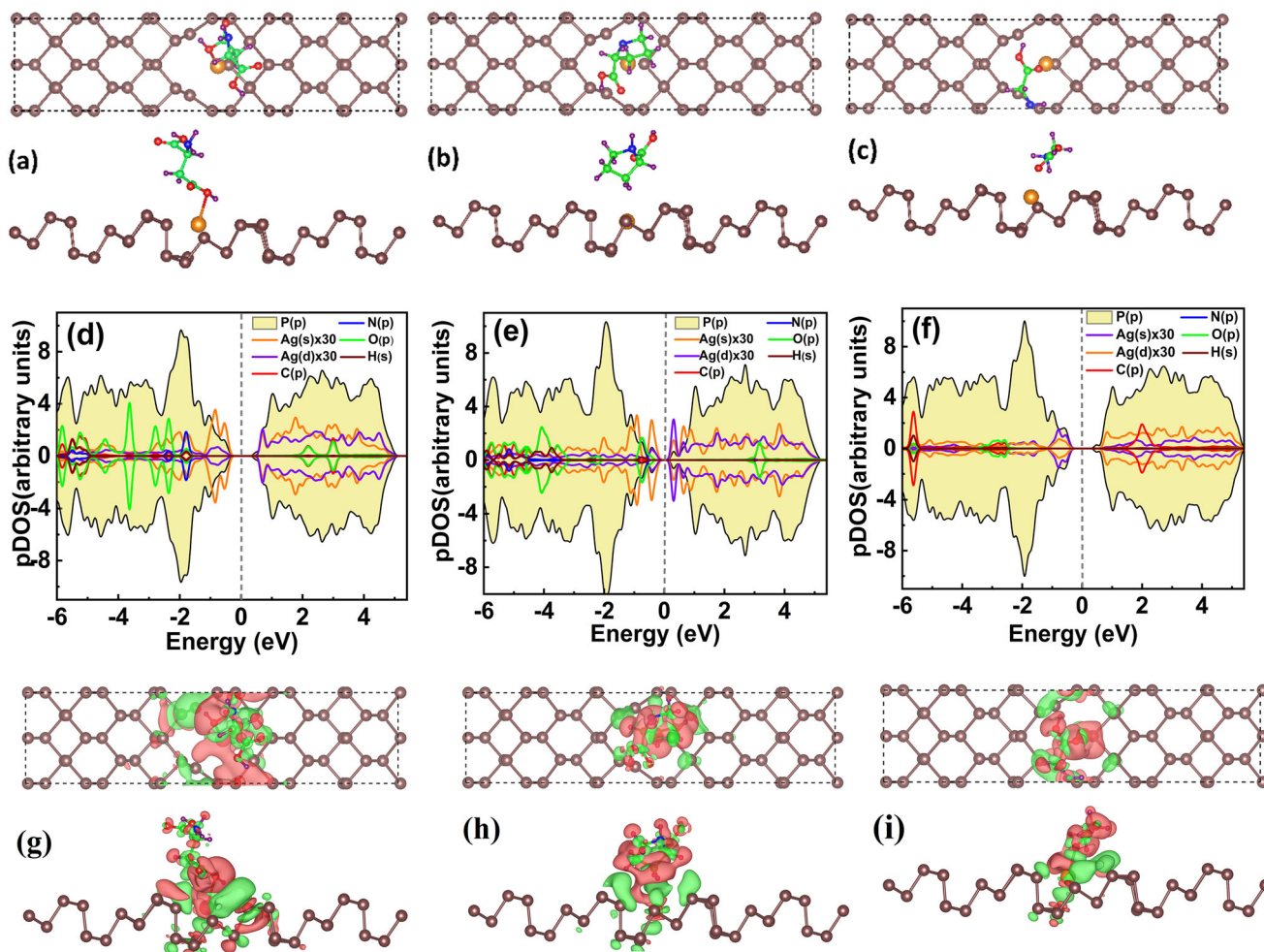
Figure 6. Optimized structures of Ag@GPM adsorbed with a) Asp, b) Pro, and c) Gly, corresponding SPDOS plots and charge density plots are presented in (d–f) and (g–i) respectively. (Brownish crimson: P, green: carbon, blue: nitrogen, red: oxygen, maroon: hydrogen, orange: Ag.)

than those on GPM and GPM_{vac}. The Bader analysis reveals a significant gain of charges by AAs. For Pro-adsorbed Ag-GPM, the impurity bands Ag-s, as well as N p and O p states, are evident near the Fermi level in the valance band region whereas Ag-d bands dominate the conduction band region (Figure 6b). In Gly adsorbed Ag@GPM, Ag-s hybridizing with P-s bands is dominating near the valance band region (Figure 6c). Though Cu@GPM and Zn@GPM also show enhanced sensitivities toward AAs, which is evident from stronger E_{ads} values as compared to the GPM and GPM_{vac} (Table 1), the improvement in E_{ads} is less pronounced compared to that of Ag@GPM. Without metal doping, the charge transfer occurs from the AA molecule to the GPM in each of the AA adsorbed systems. The AA molecule also gets heavily polarized where N and O atoms are the charge surplus group, and the C atoms become the charge deficient group. The overall dipole moment of the AAs induces physisorption at the AAs–GPM interface with a small correction due to net charge transfer. Whereas in the case of metal-doped systems, the metal

**ADVANCED
SCIENCE NEWS**

www.advancedsciencenews.com

**ADVANCED
THEORY AND
SIMULATIONS**

www.advtheorysimul.com

Figure 7. a–c) The ground state structures of all the AAs adsorbed on GPM in the H$_2$O environment.

atom (Ag, Cu, and Zn) itself loses significant amount of charge cloud and becomes cationic and plays significant anchoring entity to adsorb the polarized AAs.

3.3. Electrostatic Potential and Work Function

Upon AAs adsorption, the electrostatic potentials of GPM, GPM$_{vac}$, Ag-, Cu-, and Zn@GPM were changed due to redistribution of charge densities. The change in electrostatic potential is the variation in resistance of the monolayers, which is one of the most important parameters for the selective sensing of the AAs. Therefore, we have calculated the planner average electrostatic potentials (Vz) of GPM, GPM$_{vac}$, Ag-, Cu-, and Zn@GPM systems loaded with the AAs by Equation (3) and the results are presented in Figure S4a–c in the Supporting Information.

The redistribution of charge densities upon adsorption of AAs results in built-in electric field directed from the monolayer surfaces toward the respective AAs. The Vz values of the AAs adsorbed monolayers appear to be higher than that of the bare ones (blue arrow mark in Figure S4a–c, Supporting Information) indicating the selective sensing of AAs. The variation is found to be more significant for the Ag@GPM for all the three AAs. The substantial variation would create a sturdier internal electric field perpendicular to the Ag@GPM plane, indicating a better sensitivity toward the AAs molecules.

Further, we have calculated the work function (ω_f) as per Equation (3). The calculated ω_f of GPM, GPM$_{vac}$, Ag-, Cu-, and Zn@GPM with and without AAs are presented in Figure S5a–c in the Supporting Information. The ω_f values of GPM, GPM$_{vac}$, Ag-, Cu-, and Zn@GPM change after the adsorption of AAs. Upon AAs adsorption, one can notice a significant reduction in ω_f of Ag@GPM, whereas enhancement in ω_f for Zn@GPM. The reduction in ω_f makes Ag donates an electron to the AAs which results in enhanced adsorption energy of GPM-Ag toward Asp. However, it is the other way round for the Zn@GPM. Upon adsorption of AAs, the charge distribution creates a negative electron affinity state for the Zn@GPM, which results in a significant increase in ω_f. For both GPM and GPM$_{vac}$, a rather smaller change in ω_f occurs upon the adsorption of AAs. On the other hand, for Cu@GPM, the change in ω_f is very significant in the case of Gly compared to Asp and Pro which results in enhanced adsorption energy of Cu@GPM for Gly compared to the other two (Table 1).

3.4. Adsorption of AAs in Aqueous Medium

Since the studied AAs are present in an aqueous medium, therefore we have investigated their interaction mechanism with the GPM, GPM$_{vac}$, Ag-, Cu-, and Zn@GPM systems for practical detection purposes. For this purpose, we have considered water as a

Table 2. Adsorption energies of all AAs adsorbed on GPM, GPM$_{vac}$, and GPM-M in the H$_2$O environment.

AAs	E_{adQ}				
	GPM	GPM$_{vac}$	Ag@GPM	Cu@GPM	Zn@GPM
Asp	−0.61	−0.58	−0.37	−0.21	−0.51
Pro	−0.63	−0.51	−0.31	−0.11	−0.33
Gly	−0.67	−0.85	−0.71	−0.65	−0.15

continuous medium by using the implicit solvation method. The adsorption energy E_{adQ} in aqueous medium is estimated as

$$E_{adQ} = E_{S-AAs-Aq} - E_{S-Aq} - E_{AAs} \tag{6}$$

here the 1st and 2nd terms present the total energies (in aqueous medium) of the GPM, GPM$_{vac}$, Ag-, Cu-, and Zn@GPM loaded with and without AAs, respectively, and the 3rd term represents the energy of the individual AAs molecules. The ground-state structures of all the AAs adsorbed systems are presented in **Figure 7**a–c and Figure S6a-l in the Supporting Information, the corresponding E_{adQ} are summarized in **Table 2**.

It is clear from Table 2 that both GPM, and GPM$_{vac}$ adsorb the AAS stronger than the doped Ag-, Cu-, and Zn@GPM systems even though the average binding distances of AAs to GPM have increased slightly in aqueous medium compared to that in vacuum medium. No structural disintegration is observed for the AAs-adsorbed GPM, GPM$_{vac}$, Ag-, Cu-, Zn@GPM systems in the aqueous medium.
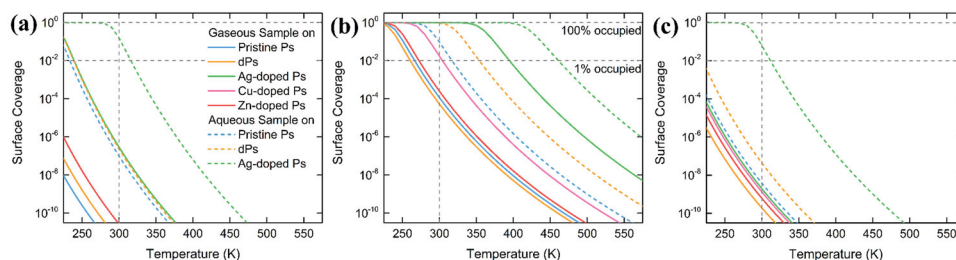
3.5. Thermodynamic Analysis

We calculated isobaric occupancies of aspartic AAs to compare the adsorptive performance of GPM, GPM$_{vac}$, Ag-, Cu-, Zn@GPM substrates as discussed above. The average number of adsorbed molecules per unit cell, in other words, surface coverage θ_X for target species, X may be calculated by following Equation (7)

$$\theta_X\,(P, T) = \frac{e^{\left(\mu_X(P,T) - E_{ads,X}\right)/k_B T}}{1 + e^{\left(\mu_X(P,T) - E_{ads,X}\right)/k_B T}} \tag{7}$$

where P and T are the pressure and the temperature of the surrounding system. Equation (7) is based on the Boltzmann statistics for classical gas. However, it can be used for the aqueous analytes in dilute concentrations.[29] The equivalent pressures of 1 mg kg^{-1} of an aqueous solution of aspartic acid, glycine, and proline are set to 187.4, 332.3, and 216.6 μbar, respectively. $\mu_X(P, T)$ indicate chemical potential of the chosen

**ADVANCED
SCIENCE NEWS**

www.advancedsciencenews.com

**ADVANCED
THEORY AND
SIMULATIONS**

www.advtheorysimul.com

Figure 8. Isobaric occupancies of a) Asp, b) Gly, and c) Pro for various GPM-based systems. The pressures of each target chemical are set to 187.4, 332.3, and 216.6 μbar for Asp, Gly, and Pro, respectively. Those pressures correspond to the concentration of 1 mg kg^{-1} of aqueous solution. The terms, "gaseous" and "aqueous" in the legend indicate whether water molecules surrounding the target molecule exist.

one in a homogenous gaseous state at a given P and T. It is obtained by single-molecule thermochemistry calculation at the ωB97XD/aug-cc-pVTZ[58,59] level of theory with IEFPCM solvation model[60] by Gaussian16 software. The real chemical potential μ_X^{real} which is estimated by thermochemistry calculation is expressed by addition of monatomic ideal gas component μ_X^{ideal} and correction terms as below Equation (8)

$$\mu_X^{real}\ (P, T) = \mu_X^{ideal}\ (P, T) + \left(A_X + B_X T + C_X T^2 \right) \qquad (8)$$

Fitted parameters in the correction term are shown in Table S3 in the Supporting Information. $E_{ads,X}$ denotes the adsorption energy which is obtained by first-principles calculation. k_B is the Boltzmann constant.

As shown in **Figure 8**, Ag@GPM exhibits superior adsorptive performances for the three AAs owing to stronger E_{ads} values. Assuming the situation that the chemical sensor based on this GPM examines the existence of those chemicals in an aqueous state, Ag@GPM could be a good choice to detect three components. Therefore, GPM, and GPM$_{vac}$ may be utilized as a Gly chemical sensor because of high-surface coverage, as depicted in Figure 8b.

In addition to the surface coverage at the given pressure and temperature, the decline of surface coverage by increasing temperature indicates the potential application of adsorbents for those species. Asp acid and Pro adsorbed on Ag@GPM at room temperature can be desorbed in mild heating as shown in Figure 8a,c. Similarly, Gly captured by GPM and GPM$_{vac}$ also can be detached as the temperature increases. In this case, as illustrated in Figure 8b, Ag@GPM cannot be used as a reversible adsorbent for Gly because of its excessively high adsorption energies.

These results mean Ag@GPM has the potential to be used as a chemical sensor for the detection of Asp, Gly, and Pro in even 1 mg kg^{-1} of dilute concentrations. Therefore, GPM and GPM$_{vac}$ can be utilized as a Gly adsorbent or chemical sensor, using the instant change of surface coverage in mild heating with suitable occupancies.

4. Summary

Inspired by the effectiveness of efficient detections of certain AAs, such as glycine (Gly), proline (Pro), and aspartic (Asp), which caused different types of flu, we performed DFT calculations coupled with thermodynamic analysis on GPMs-based nanosensor. We found that pristine (vacancy-induced) GPM

(GPM$_{vac}$) binds Gly, Pro, and Asp with adsorption energies (E_{ads}) of -0.76 (-0.74), -0.59 (-0.56), and -0.49 (-0.53) eV, respectively. However, Ag doping, at a low doping concentration of (<2%), enhanced the E_{ads} values of Ag@GPM to -1.22, -0.62, and -0.82 eV for Gly, Pro, and Asp, respectively. Other doped system, Cu@GPM, and Zn@GPM improved the E_{ads} slightly as compared to pristine GPM. We further studied the binding mechanism in aqueous medium for the practical sensing applications.

Additionally, we found distinct changes in the electronic properties, studied through DOS, electrostatic potentials, and work function calculations, of GPM, GPM$_{vac}$, and Ag@GPM upon the exposure of Gly, Pro, and Asp, which validated the promise of GPM-based nanosensor toward the studied AAs. Finally, Boltzmann thermodynamic analysis was employed to study the AAs detection mechanism at varied conditions of pressure and temperatures. We strongly believe that the distinctive and tunable electrochemistry of GPM will be advantageous for developing nanobiosensors for the early detection of viral flu-like infections with high sensitivity and selectivity.

Supporting Information

Supporting Information is available from the Wiley Online Library or from the author.

Conflict of Interest

The authors declare no conflict of interest.

Data Availability Statement

The data that support the findings of this study are available from the corresponding author upon reasonable request.

Keywords

binding, dopants, monolayer, phosphorene, thermodynamic analysis

[1] S. Li, L. Ma, M. Zhou, Y. Li, Y. Xia, X. Fan, C. Cheng, H. Luo, *Curr. Opin. Biomed. Eng.* **2020**, *13*, 32.
[2] A. Bolotsky, D. Butler, C. Dong, K. Gerace, N. R. Glavin, C. Muratore, J. A. Robinson, A. Ebrahimi, *ACS Nano* **2019**, *13*, 9781.
[3] S. Kumar, Y. Lei, N. H. Alshareef, M. A. Quevedo-Lopez, K. N. Salama, *Biosens. Bioelectron.* **2018**, *121*, 243.
[4] M. Samprathi, M. Jayashree, *Front. Pediatr.* **2021**, *8*, 607647.
[5] D. R. Wessner, *Nat. Educ.* **2010**, *3*, 61.
[6] J. Louten, in *Essential Human Virology* (Ed: J. Louten), Elsevier, New York **2016**, pp. 19–29.
[7] J. Zhang, Y. Cai, T. Xiao, J. Lu, H. Peng, S. M. Sterling, R. M. Walsh, S. Rits-Volloch, H. Zhu, A. N. Woosley, W. Yang, P. Sliz, B. Chen, *Science* **2021**, *372*, 525.
[8] M. Becerra-Flores, T. Cardozo, *Int. J. Clin. Pract.* **2020**, *74*, e13525.
[9] C. B. Jackson, M. Farzan, B. Chen, H. Choe, *Nat. Rev. Mol. Cell Biol.* **2022**, *23*, 3.
[10] B. Sajjanar, B. Kakodia, D. Bisht, S. Saxena, A. K. Singh, V. Joshi, A. K. Tiwari, S. Kumar, *J. Nanopart. Res.* **2015**, *17*, 234.
[11] J. Lee, M. Morita, K. Takemura, E. Y. Park, *Biosens. Bioelectron.* **2018**, *102*, 425.
[12] A. Mokhtarzadeh, R. Eivazzadeh-Keihan, P. Pashazadeh, M. Hejazi, N. Gharaatifar, M. Hasanzadeh, B. Baradaran, M. de la Guardia, *TrAC, Trends Anal. Chem.* **2017**, *97*, 445.
[13] C. Sharma, S. Walia, A. Acharya, in *Nanomaterial-Based Biomedical Applications in Molecular Imaging, Diagnostics and Therapy* (Ed: A. Acharya), Springer, Singapore, Singapore **2020**, pp. 55–77.
[14] N. Rohaizad, C. C. Mayorga-Martinez, M. Fojtů, N. M. Latiff, M. Pumera, *Chem. Soc. Rev.* **2021**, *50*, 619.
[15] D. Chimene, D. L. Alge, A. K. Gaharwar, *Adv. Mater.* **2015**, *27*, 7261.
[16] Y. Shao, J. Wang, H. Wu, J. Liu, I. A. Aksay, Y. Lin, *Electroanalysis* **2010**, *22*, 1027.
[17] Y. Wang, Y. Shao, D. W. Matson, J. Li, Y. Lin, *ACS Nano* **2010**, *4*, 1790.
[18] A. Bolotsky, D. Butler, C. Dong, K. Gerace, N. R. Glavin, C. Muratore, J. A. Robinson, A. Ebrahimi, *ACS Nano* **2019**, *13*, 9781.
[19] X. Chen, J. Zhu, Q. Xi, W. Yang, *Sens. Actuators, B* **2012**, *161*, 648.
[20] L. Han, C.-M. Liu, S.-L. Dong, C.-X. Du, X.-Y. Zhang, L.-H. Li, Y. Wei, *Biosens. Bioelectron.* **2017**, *87*, 466.
[21] L. Wu, X. Lu, X. Fu, L. Wu, H. Liu, *Sci. Rep.* **2017**, *7*, 5191.
[22] S. K. Krishnan, E. Singh, P. Singh, M. Meyyappan, H. S. Nalwa, *RSC Adv.* **2019**, *9*, 8778.
[23] I.-H. Cho, D. H. Kim, S. Park, *Biomater. Res.* **2020**, *24*, 6.
[24] B. He, T. J. Morrow, C. D. Keating, *Curr. Opin. Chem. Biol.* **2008**, *12*, 522.
[25] A. N. Sokolov, M. E. Roberts, Z. Bao, *Mater. Today* **2009**, *12*, 12.
[26] Md. Z. H. Khan, *Cogent Eng.* **2016**, *3*, 1170097.
[27] C. Ménard-Moyon, A. Bianco, K. Kalantar-Zadeh, *ACS Sens.* **2020**, *5*, 3739.
[28] P. Panigrahi, A. K. Dhinakaran, Y. Sekar, R. Ahuja, T. Hussain, *ChemPhysChem* **2018**, *19*, 2250.
[29] P. Panigrahi, D. Jini, H. Bae, H. Lee, R. Ahuja, T. Hussain, *Appl. Surf. Sci.* **2021**, *542*, 148590.
[30] Z. Li, S. L. Wong, *Mater. Sci. Eng., C* **2017**, *70*, 1095.
[31] Q. Ouyang, S. Zeng, L. Jiang, J. Qu, X.-Q. Dinh, J. Qian, S. He, P. Coquet, K.-T. Yong, *J. Phys. Chem. C* **2017**, *121*, 6282.
[32] Y. J. Park, B. K. Sharma, S. M. Shinde, M.-S. Kim, B. Jang, J.-H. Kim, J.-H. Ahn, *ACS Nano* **2019**, *13*, 3023.
[33] H. Riazi, G. Taghizadeh, M. Soroush, *ACS Omega* **2021**, *6*, 11103.
[34] Y. Zhou, J. Yoon, *Chem. Soc. Rev.* **2012**, *41*, 52.
[35] G. Patel, S. Menon, *Chem. Commun.* **2009**, 3563.
[36] E. Badetti, L. Calgaro, L. Falchi, A. Bonetto, C. Bettiol, E. Leonetti, E. Ambrosi, E. Zendri, A. Marcomini, *Nanomaterials* **2019**, *9*, 792.
[37] M. Maatallah, A. Jarid, *Chem. Phys.* **2019**, *516*, 103.
[38] L. Kou, T. Frauenheim, C. Chen, *J. Phys. Chem. Lett.* **2014**, *5*, 2675.
[39] J. M. Marmolejo-Tejada, A. Jaramillo-Botero, *Phys. Chem. Chem. Phys.* **2019**, *21*, 19083.
[40] S. Cui, H. Pu, S. A. Wells, Z. Wen, S. Mao, J. Chang, M. C. Hersam, J. Chen, *Nat. Commun.* **2015**, *6*, 8632.
[41] L. Zhou, C. Liu, Z. Sun, H. Mao, L. Zhang, X. Yu, J. Zhao, X. Chen, *Biosens. Bioelectron.* **2019**, *137*, 140.
[42] S. Kaur, A. Kumar, S. Srivastava, K. Tankeshwar, R. Pandey, *J. Phys. Chem. C* **2018**, *122*, 26032.
[43] T. Kaewmaraya, L. Ngamwongwan, P. Moontragoon, W. Jarernboon, D. Singh, R. Ahuja, A. Karton, T. Hussain, *J. Hazard. Mater.* **2021**, *401*, 123340.
[44] P. E. Blöchl, *Phys. Rev. B* **1994**, *50*, 17953.
[45] G. Kresse, J. Furthmüller, *Comput. Mater. Sci.* **1996**, *6*, 15.
[46] G. Kresse, J. Furthmüller, *Phys. Rev. B* **1996**, *54*, 11169.
[47] G. Kresse, D. Joubert, *Phys. Rev. B* **1999**, *59*, 1758.
[48] J. P. Perdew, K. Burke, M. Ernzerhof, *Phys. Rev. Lett.* **1996**, *77*, 3865.
[49] S. Grimme, *J. Comput. Chem.* **2006**, *27*, 1787.
[50] H. J. Monkhorst, J. D. Pack, *Phys. Rev. B* **1976**, *13*, 5188.
[51] P. C. Rusu, G. Brocks, *J. Phys. Chem. B* **2006**, *110*, 22628.
[52] K. Mathew, R. Sundararaman, K. Letchworth-Weaver, T. A. Arias, R. G. Hennig, *J. Chem. Phys.* **2014**, *140*, 084106.
[53] J. Hao, Z. Wang, Q. Jin, *Sci. Rep.* **2019**, *9*, 11264.
[54] K. T. Chan, J. B. Neaton, M. L. Cohen, *Phys. Rev. B* **2008**, *77*, 235430.
[55] J. Woo, K.-H. Yun, S. B. Cho, Y.-C. Chung, *Phys. Chem. Chem. Phys.* **2014**, *16*, 13477.
[56] Y. Cai, G. Zhang, Y.-W. Zhang, *J. Phys. Chem. C* **2017**, *121*, 10182.
[57] D. Burman, H. Raha, B. Manna, P. Pramanik, P. K. Guha, *ACS Sens.* **2021**, *6*, 3398.
[58] J.-D. Chai, M. Head-Gordon, *J. Chem. Phys.* **2008**, *128*, 084106.
[59] J.-D. Chai, M. Head-Gordon, *Phys. Chem. Chem. Phys.* **2008**, *10*, 6615.
[60] A. V. Marenich, C. J. Cramer, D. G. Truhlar, *J. Phys. Chem. B* **2009**, *113*, 6378.